THE JOURNAL OF PHYSICAL CHEMISTRY A

ARTICLE

pubs.acs.org/JPCA

Aqua Ions—Graphene Interfacial and Confinement Behavior: Insights from Isobaric—Isothermal Molecular Dynamics

Ariel A. Chialvo*[,†] and Peter T. Cummings[‡,§]

[†]Chemical Sciences Division, Geochemistry and Interfacial Sciences Group, Oak Ridge National Laboratory, Oak Ridge, Tennessee 37831-6110, United States

[‡]Department of Chemical and Biomolecular Engineering, Vanderbilt University, Nashville, Tennessee 37235-1604, United States

[§]Nanomaterials Theory Institute, Center for Nanophase Materials Sciences, Oak Ridge National Laboratory, Oak Ridge, Tennessee 37831-6494, United States

S Supporting Information

ABSTRACT: We carry out a systematic microstructural characterization of the solid—fluid interface (SFI) of water and simple metal chloride aqueous solutions in contact with a free-standing plate or with two such plates separated by an interplate distance $0 \leq h$ (Å) ≤ 30 at ambient conditions via isothermal—isobaric molecular dynamics. With this characterization, we target the interrogation of the system in search for answers to fundamental questions regarding the structure of the "external" and "internal" (confined) SFIs, the effect of the differential hydration behavior among species, and its link to species expulsion from confinement. For water at ambient conditions, we found that the structure of the "external" SFIs is independent of the interplate distance h in the range $0 \leq h$ (Å) ≤ 30, that is, the absence of wall-mediated correlation effects between "external" and "internal" SFIs, and that for $h < 9$ Å the slit-pores dewet. Moreover, we observed a selective expulsion of ions caused by the differential hydration between the anion and the cations with a consequent charging of the slit-pore. All these observations were interpreted in terms of the axial profiles for precisely defined order parameters, including tetrahedral configuration, hydrogen bonding, and species coordination numbers.

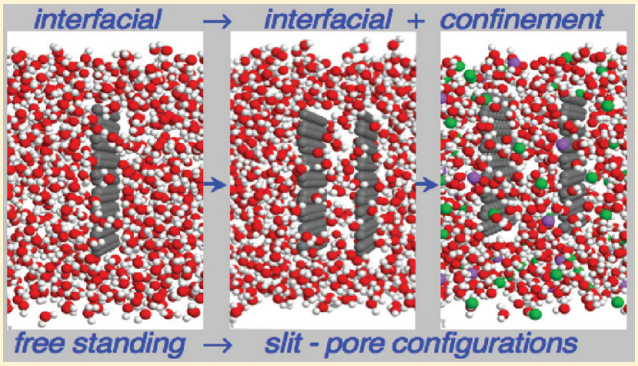

1. INTRODUCTION

The behavior of water at water—solid interfaces has been the focus of an extensive research effort involving theoretical,[1−3] simulation,[4−11] and experimental[12−17] approaches that confirmed our expectation that water's structural and dynamic properties are modified at the interfacial region.[18,19] This expectation is based on the fact that the insertion of a solid surface into an otherwise homogeneous bulk fluid brings in an obvious interaction asymmetry between the fluid—surface and the fluid—fluid interactions whose competition can lead to a gamut of interfacial phenomena.

To gain valuable insight into the interfacial behavior of aqueous systems in contact with solid surfaces, we can invoke the solvation analogy that describes an immersed surface as a very large (and fixed in space) infinitely dilute solute particle whose interaction with the surrounding fluid induces a propagating local density perturbation across the system.[20] This density perturbation translates into inhomogeneous distributions of the fluid properties that would decay to their corresponding bulk values as long as the fluid does not encounter or overlap another inhomogeneous region with the consequent formation of confinement.

Depending on the asymmetry between the water—water and water—surface interactions, in addition to the nature of the solid surface (i.e., size/shape,[21−23] topography/texture,[10,24,25] and polarity[26,27]) and the presence of other species,[28] we might encounter different hydration structures near water—solid interfaces that are usually described in terms of the hydrophilic or hydrophobic nature of the surfaces. In fact, Lum et al.[2] provided a theoretical approach to describe how significant the differences are of hydrophobic interactions between small apolar solutes and those between sufficiently large polar groups. The differences between these two regimes were rationalized in terms of the dominant driving forces behind the corresponding hydration processes, that is, bulk water properties and entropic (water's structural perturbation) contributions dominate the hydration process of small solutes, while interfacial water properties and (water—solute) enthalpic contributions control hydration for larger solutes. These two hydration regimes exhibit a crossover at a nanometer length scale,[2] where the key player behind this

Special Issue: Victoria Buch Memorial

Received: October 28, 2010
Revised: April 4, 2011

 © XXXX American Chemical Society

phenomenon is the ability of water to reorganize its hydrogen-bonded network around apolar groups. From a geometric standpoint, water is more likely to encapsulate small apolar solutes than larger apolar bodies, with no significant perturbation of its hydrogen-bonded network. From an energetic perspective, the enthalpic effect resulting from the disruption of water's hydrogen-bond network in contact with extended hydrophobic plates can induce interplate drying (dewetting), that is, the loss of hydrogen bonding interactions can destabilize the confined water, resulting in the formation of vapor-like environments.[1]

Because ions can exhibit strong binding with water they also affect the hydrogen bonding within their hydration shells.[29−31] Consequently, we should expect significant differences between the interfacial/confined behavior of water and aqueous electrolytes, depending on the charge and size of the ionic species present. Under these circumstances, it appears essential for the understanding of SFI's structure to address the hydration behavior of simple ions, their impact on the tetrahedral distribution of the surrounding water, and its associated effect on the hydrogen-bonding network in these inhomogeneous aqueous environments.

The present work has been motivated in part by, and should be put in the context of, recent experimental evidence by EXAFS analysis[32] and subsequent molecular-based simulation interpretation[33] of the alleged partial dehydration of Rb^+ and Ca^{2+} in aqueous solution confined in carbon nanopores with respect to the corresponding bulk counterparts. Consequently, the aim of this work is the systematic characterization of the structure of SFIs comprising water and simple electrolyte solutions of metal chlorides in contact with free-standing graphene plates or under pronounced confinement between finite-size uncharged graphene plates at ambient conditions. This characterization is intended to address the following fundamental questions: (a) To what extent does the structure of the "external" SFIs differ from that of the corresponding "internal" or confined SFIs? (b) Is there any wall-mediated correlation effect between "external" and "internal" SFIs? (c) How does the differential hydration behavior among species affect the resulting SFIs? (d) What is the link between differential ionic species expulsion and the local electroneutrality condition in a slit pore?

To tackle the proposed questions, we perform extensive molecular dynamics simulations of precisely defined model systems, including the atomistic explicit description of the aqueous solutions and the graphene plates, according to the models and methodology presented in section 2. In section 3, we present the simulated microstructural results in terms of the full characterization of the inhomogeneous SFI's environments. Finally, in section 4, we discuss the significance of our work in the context of relevant experimental evidence and provide an outlook.

2. MODELS AND SIMULATION APPROACH

To study the behavior of water and aqueous electrolytes at the fluid-graphene interfaces (free-standing plates) and under confinement between graphene plates (finite-size slit-pore), we performed isobaric−isothermal molecular dynamics simulations of aqueous metal chloride solutions involving mono-, di-, and trivalent cations at ambient conditions. For that purpose, we have chosen simple but reliable intermolecular potential models including the rigid SPC/E water model,[34] with Dang's,[35,36] Aqvist's,[37] and Bowron's[38] parametrizations for lithium, chloride, barium, and yttrium interactions with SPC/E water, respectively. All these potentials are represented in terms of Lennard-Jones (LJ) and electrostatic interactions, while the unlike LJ-pair interactions are described by the Lorentz−Berthelot combining rules (Table 1). We chose these metal ions because their potential parameters follow a quasi-linear dependence with the cation's electrostatic charge (Figure 1), a feature that facilitates later the interpretation of simulation results.

Table 1. Lennard-Jones Potential Parameters and Partial Charges for the Ion−Ion and Water−Water Interactions[a]

ii-interaction	ε_{ii}/k (*K*)	σ_{ii} (Å)	q_i (*e*)	ref
O−O	78.23	3.166	−0.8476	34
Li−Li	83.04	1.508	1.0	35
Ba−Ba	50.34	2.050	2.0	37
Y−Y	15.04	3.100	3.0	38
Cl−Cl	50.34	4.400	− 1.0	35

[a] Unlike-pair interaction parameters are based on Lorentz−Berthelot combining rules.

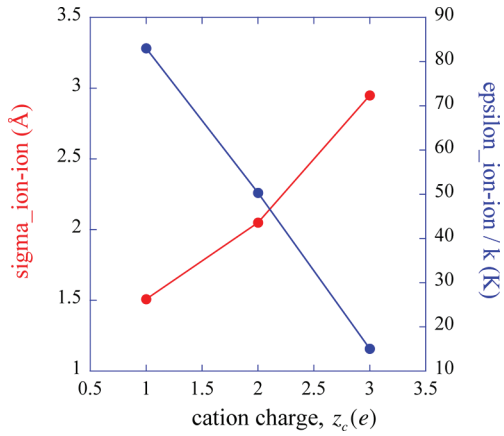

Figure 1. Dependence between the Lennard-Jones parameters of the metal cations used in this study and their electrostatic charge.

The isobaric−isothermal molecular dynamics simulations of water and the aqueous solutions were carried out according to our own implementation of a Nosé-Poincare symplectic integration algorithm[39,40] with a time-step of 2.0 fs. The fluid environment consists of either pure water or 2*m* metal chloride aqueous solutions and comprises a total of 2048 particles (i.e., 2048, N_{ions} water molecules plus $N_{ions} = (1 + z_c)N_{Cl^-}$, where z_c is the cation's electrostatic charge) at T = 298 K and P = 1 atm within a tetragonal, $\mathbb{L}_z = 2\mathbb{L}_x = 2\mathbb{L}_y$, simulation box subject to 3D periodic boundary conditions. The simulation cell contains either a single graphene plate (Figure 2, top) or two identical (in registry) graphene plates are immersed approximately equidistant from the center of the box while kept fixed in space and separated by a distance $6 \leq h$ (Å) ≤ 30 (slit pore configuration, Figure 2, bottom) during the simulation. Each graphene plate comprises 136 carbon sites explicitly described as Lennard-Jones spheres in the $X-Y$ plane, characterized by $\varepsilon_{CC}/k = 28K$ and $\sigma_{CC} = 3.40$ Å[41−43] and an adjacent carbon−carbon distance of 1.42 Å, that is, 17.04 Å by 18.44 Å, where these dimensions are always smaller than the $X-Y$ dimensions of the fluctuating system volume. Consequently, the environment in the two sides of a free-standing graphene plate, or that in the confined space between graphene plates, is able to exchange species with the surrounding, that is, behaving effectively as a grand canonical (open) system.

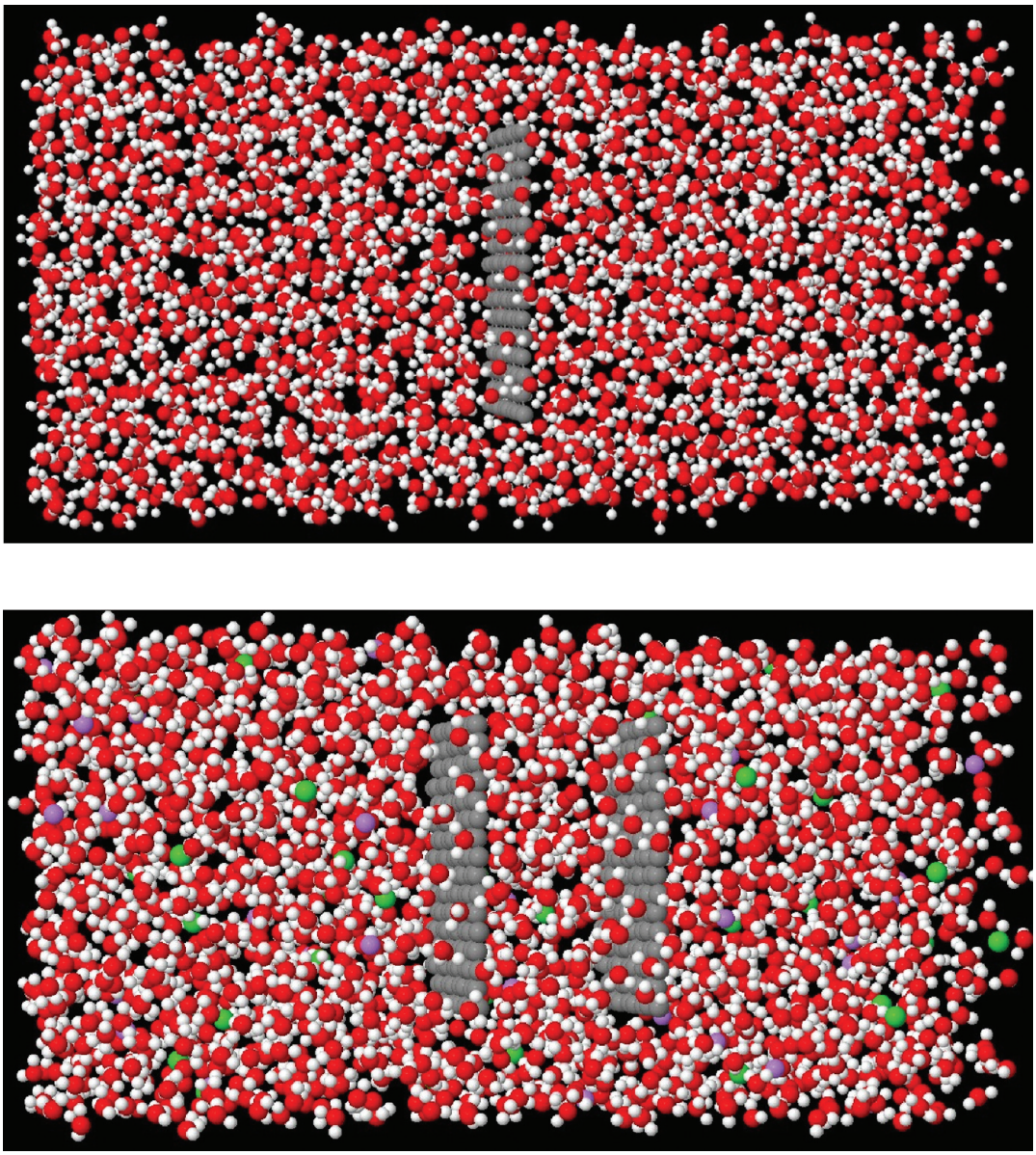

Figure 2. Typical simulation box configurations for a free-standing plate in pure water (top) and a slit pore immersed in a 2 m LiCl aqueous solution (bottom).

In other words, this simulation box scheme allows us to analyze simultaneously the confined fluid behavior in equilibrium with its corresponding bulk at precisely the same global state conditions.

The tetragonal simulation box was chosen because it allows us to analyze simultaneously the pure interfacial ("external") and the confined ("internal", i.e., the overlapping between interfaces of approaching graphene plates) behavior of the aqueous environments. The analysis of the behavior of a purely interfacial free-standing plate compared with that corresponding to the interfacial-confined slit-pore counterpart is aimed at detecting potential correlation effects between the confined fluid and the two interfacial regions outside the slit-pore. Initial simulations were started from *fcc* structures for the location of the solution species' centers of mass, while the graphene plates were intercalated between *fcc* planes, and the ionic species were randomly distributed among all *fcc* sites. All simulations comprised about 2 ns (pure water) to 12 ns (aqueous electrolytes) of phase space trajectory after a 0.5 ns equilibration from the initial *fcc* configuration, while 10^4 equilibrium system configurations were dumped for additional processing. To verify an adequate equilibration and loss of correlation with the initial system configuration we determined the residence time of the water molecules on the first coordination of the Y^{3+},[44] and the system's configurational temperature.[45,46] The estimated residence time $\tau_{Y^{3+}}{}^{S} \sim 400$ ps, thus, for the chosen simulation length $t > 30\tau_{Y^{3+}}{}^{S}$, we ensured that the water molecules have lost any correlation with the central ion. Moreover, we performed a few longer runs ($\sim$50 ns, i.e., $t > 120\tau_{Y^{3+}}{}^{S}$) for the aqueous YCl_3 systems with $h = 15$ Å and $h = 9$ Å to confirm that the observed long-ranged structures are actually equilibrated and independent of the initial system configuration.

All interactions were truncated at a cutoff radius $r_c \approx 4.5\sigma_{OO}$, the electrostatic interactions were accounted for by an Ewald summation whose convergence parameters were chosen to obtain an error smaller than $510^{-5}\varepsilon_{OO}$ for both the real and

reciprocal spaces,[47] and the configurational energy and virial were corrected by the corresponding long-range contributions.

To characterize the structure of the graphene−aqueous interfaces, both inside and outside the slit-pore, and to interpret the behavior of the resulting electric double layer, we determine the relevant axial profiles perpendicular to the graphene plate-(s), including all species densities $\rho_i(z)$, the corresponding Coulombic charge density $\rho_Q(z)$, and the relative orientation of the water molecules $\rho_\theta(z)$ as follows

$$P(z) \equiv \langle (L_x L_y \Delta)^{-1} \sum_i P_i B_c(z_i, -0.5\Delta, 0.5\Delta) \rangle \qquad (2)$$

for which P_i denotes $\delta(z - z_i)$, the Coulombic charge q_i, and the angle $\theta = \cos^{-1}(\boldsymbol{\mu}_i \cdot \hat{z}/|\boldsymbol{\mu}_i|)$, respectively, where $\boldsymbol{\mu}_i$ is the dipole moment of the water molecule i, L_α represents the size of the graphene plate along the α-axis, $\Delta \sim 0.025\sigma_{OO}$ is the bin-size, $B_c(x,a,b) \equiv [\Theta(x - a) - \Theta(x - b)]$ is the "boxcar" function,[48] $\delta(\cdots)$ is the Dirac delta function, $\Theta(\cdots)$ is the Heaviside function, and $\langle \cdots \rangle$ indicates a time average over the simulation trajectory.

In particular, the axial profile of the charge density $\rho_Q(z)$ plays a central role in this analysis, because the integration of the associated one-dimensional Poisson equation provides the corresponding profiles for the local electric field and potential, and affords the opportunity to assess (a) how confinement might affect the local compliance of electroneutrality as well as (b) how effective the solution screens any surface charge when the possibility of either overcharging or surface charge reversal might occur.[43] For further insights into the inhomogeneous fluid environment, we also analyze the axial profiles of local water packing and its hydrogen bonding behavior. For that purpose, we characterize the water packing in terms of the local tetrahedral order parameter $q_T(z_i)$ introduced by Chau and Hardwick[49] (later normalized by Errington and Debenedetti[50]), that is,

$$q_T(z) \equiv 1 - \langle (N(z))^{-1} \sum_i P_i B_c(z_i, -0.5\Delta, 0.5\Delta) \rangle;$$
$$\forall\ i(0 \le x_i \le L_x,\ 0 \le y_i \le L_y) \qquad (3)$$

where $P_i = (3/8)\Sigma_{j=1}^{3}\Sigma_{k=j+1}^{4}(\cos\phi_{ijk} - \cos(109.47°))^2$, $N(z) = \Delta\Sigma_i\delta(z - z_i)B_c(z_i, -0.5\Delta, 0.5\Delta)$, with $\Delta \sim 0.12\sigma_{OO}$, $\cos\phi_{ijk} = r_{ij} \cdot r_{ik}/(r_{ij}r_{ik})$, $109.47° = \cos^{-1}(-1/3)$ is the tetrahedral angle, the double summation comprises the four nearest neighbors (j,k) of the water molecule located at the axial distance z_i, and the angle brackets denote time average over the simulation trajectory. Note that according to the normalized eq 3 a system with a perfect tetrahedral distribution of water oxygens would exhibit $q_T = 1$; in contrast, a totally uncorrelated system would mean $q_T = 0$. Simultaneously, by taking advantage of the sorting of pair-distances during the calculation of $q_T(z)$, we also determine the corresponding axial profiles of the water coordination numbers around water and the ionic species, $n_{Oi}(z,r_c^i)$, based on the number of nearest-neighbors within a specified shell radius r_c^i given by the location of the first valley of the corresponding radial distribution function $g_{Oi}(r)$, as indicated in Table 2.

For the hydrogen bonding counterpart we use the $r\beta$-geometric definition[51] based on Wernet et al.'s interpretation of X-ray absorption spectroscopy that involves a pair of water molecules whose oxygen sites are separated by a distance $r_{OO}(\beta) = 3.3 - 0.00044\beta^2$ (Å), where the angle β (degrees) $\equiv \angle H_\alpha{-}O_\alpha \cdots O_\gamma$ is given by the intramolecular $O_\alpha{-}H_\alpha$ bond vector on molecule α and the intermolecular $O_\alpha \cdots O_\gamma$ vector formed with molecule γ.[52]

Table 2. Radius of the First Hydration Shell of Species in Solution

Oi-interaction	r_c^i (Å)	ref
O−O	∼3.33	34
O−Li^+	∼2.65	35
O−Ba^{2+}	∼3.65	37
O−Y^{3+}	∼3.5	38
O−Cl^-	∼3.8	35

3. DISCUSSION OF SIMULATION RESULTS

In this section we discuss the graphene/fluid interfacial behavior of water and aqueous electrolyte systems for free-standing graphene plates or graphene slit-pore configurations, placing emphasis on the microstructural differences between the interfacial and confined regions, and the potential effect of confinement on the species solvation and hydrogen-bond network. To aid the interpretation of the interfacial/confined behavior of aqueous electrolytes systems within the range of interplate separation $9 \le h$ (Å) ≤ 15, we have performed additional simulations involving pure water for a wider range of confinement, that is, $0 \le h$ (Å) ≤ 30 (see Table 3), at the same state conditions as for the aqueous systems. The rationale behind these additional runs will become evident in the next sections.

3.1. External versus Internal Graphene−Water Interfacial Regions. To interpret the impact of the graphene plates on the graphene-aqueous interface structure, we first analyze the systems comprising pure water for six interplate separations, i.e., h (Å) = {0, 6, 9, 12, 15, 30}, where $h = 0$ actually describes the special case of a free-standing graphene plate (Figure 2, top). Figure 3a,b, as a representative example, displays the axial profiles describing the water structure (i.e., oxygen and hydrogen sites) and corresponding relative orientation of the water's dipole moment, $\theta = \cos^{-1}(\boldsymbol{\mu}_i \cdot \hat{z}/|\boldsymbol{\mu}_i|)$, as well as the resulting pair of symmetric "external" SFIs comprising three water layers that are separated from the graphene surface by an ∼2.5 Å thick excluded volume, similar to that predicted by the first principle simulation

Table 3. Systems, Interplate Separations, and Resulting Global Densities at $T = 298K$ and $P = 1$ atm

system	$h = 0^a$ ρ (g/cm^3)^b	$h = 6$ Å ρ (g/cm^3)	$h = 9$ Å ρ (g/cm^3)	$h = 12$ Å ρ (g/cm^3)	$h = 15$ Å ρ (g/cm^3)	$h = 30$ Å ρ (g/cm^3)
LiCl + water			0.907(1)	0.909(1)	0.909(1)	
$BaCl_2$ + water			1.101(1)	1.100(1)	1.103(2)	
YCl_3 + water			1.006(2)	1.007(2)	1.006(2)	
pure water	0.974(1)	0.937(1)	0.950(1)	0.950(1)	0.951(1)	0.952(1)

[a] Free standing graphene plate. [b] Resulting global fluid density from the NPT-MD simulation.

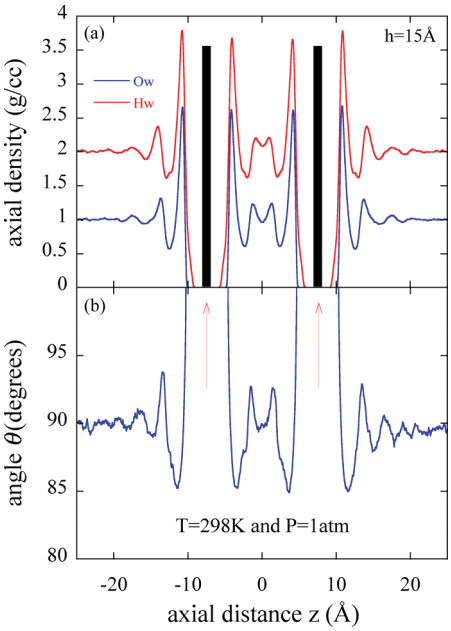

Figure 3. Axial density and orientation profiles for water interfacing planar graphene plates in a slit-pore configuration with an interplate separation h = 15 Å at T = 298 K and P = 1 atm. Red arrows and black thick vertical lines indicate the location of the plates.

of Cicero et al.[9] This external layering develops within ∼12 Å from the graphene surface beyond which water loses completely its axial structure.

Moreover, according to the relative axial location of the oxygen and hydrogen peaks, Figure 3a, the water molecules in these layers sit preferably with their molecular planes roughly parallel to the graphene plates. Note, however, that, according to the angle θ profile, Figure 3b, the relative orientation of the interfacial water molecules oscillate around the average normal dipolar orientation yet exhibiting a small tilt of one of the water hydrogens toward the graphene plates.

In Figure 4, we display the evolution of the axial density profiles for the oxygen and hydrogen sites of pure water in contact with, and confined between, graphene plates under the same external condition of T = 298 K and P = 1 atm. This picture illustrates the contrasting behavior between the external and internal interfacial regions as we change the interplate separation h and, in particular, the prima facie lack of h-dependence of the external site's density profiles compared with the profound changes of the corresponding internal ones. Moreover, it introduces the analysis of the first issue, that is, question (a) of the Introduction, because if we replot those water density profiles by shifting the axial coordinates by precisely $\pm 0.5h$, then we can compare all profiles corresponding to the left (right) external interfaces using a common axial origin as illustrated in Figure 5a−c. With regard to issue (b) in the Introduction, this comparison provides evidence that, in principle, the inhomogeneous distribution of water in the "external" SFI is not affected by the corresponding water interplate confinement (internal SFIs). This behavior contrasts greatly with that observed by Lozada Cassou et al.[53] in rather simpler fluids in contact with and under confinement between finite-width plates, such as those involving hard-spheres plus Yukawa tails, which exhibit significant fluid correlation across the slit-pore walls with changes in the interplate separation as illustrated by Monte Carlo simulations and

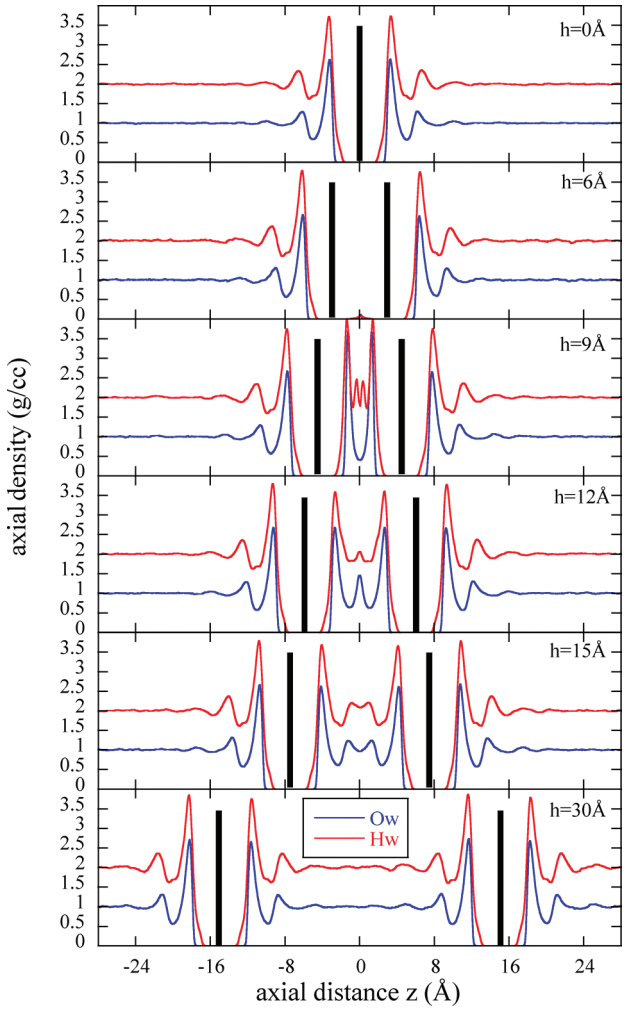

Figure 4. Axial site-density profiles for water interfacing planar graphene plates in the free-standing and slit-pore configuration within the range of interplate separations $0 \leq h$ (Å) ≤ 30 at T = 298 K and P = 1 atm.

HNC integral equation calculations. Moreover, we note that because the distance between the peaks of the first adsorbed water layer on the two sides of a graphene plate is ∼7 Å $\ll r_c$, we should expect non-negligible graphene mediated water−water (Lennard-Jones plus electrostatic) interactions, and, consequently, the likelihood of correlation effects between the internal and external interfacial structures, especially at plate separations where dewetting occurs.

Additional structural evidence for the lack of (or negligible) correlation (issue b) is given in Figure 6a−c, where we compare the resulting axial profiles for the average tetrahedral order parameter $q_T(z)$, number of hydrogen bonds per molecule $n_{HB}(z)$, and corresponding first coordination number $n_{OO}(z)$ within the external interfaces for $0 \leq h$ (Å) ≤ 30. The behavior of these three properties is very similar to one another and unaffected by the interplate separation h, that is, they exhibit a couple of mild peaks at ∼4.8 Å and 7.8 Å for $q_T(z)$, ∼5.3 Å and 7.8 Å for $n_{HB}(z)$, as well as ∼5.5 Å and 8.3 Å for $n_{OO}(z)$, respectively, beyond which these quantities take their known bulk values.[50,51,54,55] The observed similarity is not surprising since the three quantities are interrelated descriptors of the water ability to form hydrogen-bonded networks. Moreover, note that

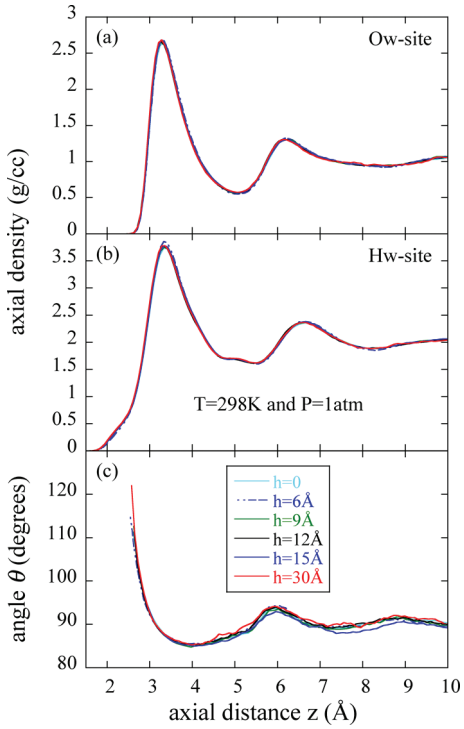

Figure 5. Shifted (superimposed) site-densities (a,b) and molecular orientation (c) axial profiles for water interfacing planar graphene plates in the free-standing and slit-pore configuration within the range of interplate separations $0 \leq h$ (Å) ≤ 30 at $T = 298$ K and $P = 1$ atm.

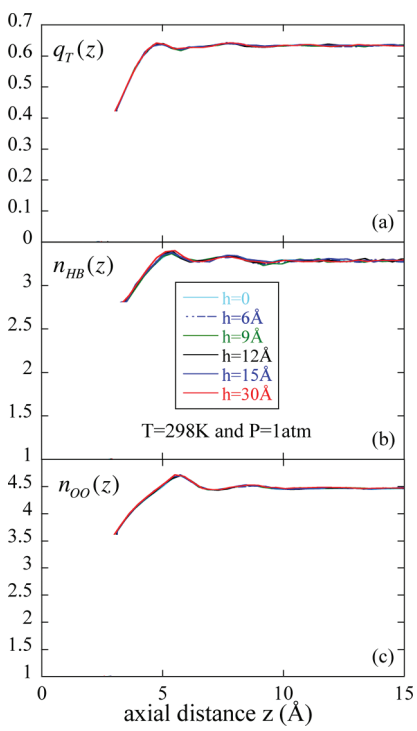

Figure 6. Shifted (superimposed) axial profiles of (a) $q_T(z)$, (b) $n_{HB}(z)$, and (c) $n_{OO}(z)$ for water interfacing planar graphene plates in the free-standing and slit-pore configuration within the range of interplate separations $0 \leq h$ (Å) ≤ 30 at $T = 298$ K and $P = 1$ atm.

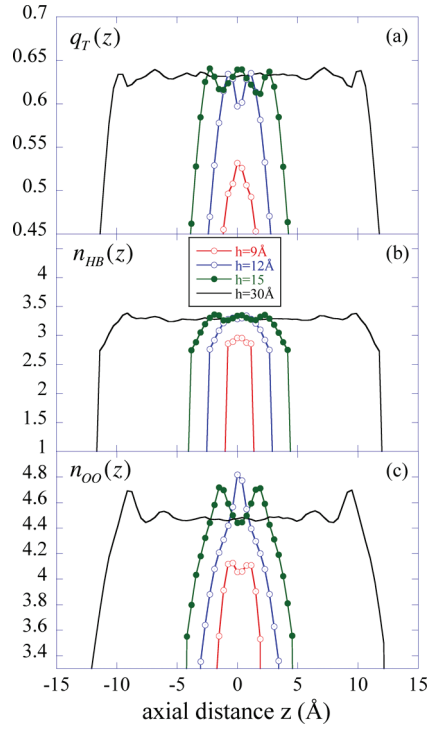

Figure 7. Axial profiles of (a) $q_T(z)$, (b) $n_{HB}(z)$, and (c) $n_{OO}(z)$ for confined water interfacing planar graphene plates in the slit-pore configuration within the range of interplate separations $0 \leq h$ (Å) ≤ 30 at $T = 298$ K and $P = 1$ atm.

this ability (and correspondingly, the strength of $q_T(z)$, $n_{HB}(z)$, and $n_{OO}(z)$) decreases dramatically at the first adsorbed water layer centered at ~3.3 Å, due to the spatial constraint imposed by the graphene surface and consequent disruption of the hydrogen bonding.

In contrast to the "external" SFI behavior (Figures 5 and 6), the interfacial structure of the confined water is strongly affected by the interplate separation h as a direct consequence of the partial overlapping (i.e., either constructive or destructive interference) of the approaching interfacial structures from opposite graphene plates (Figure 4). On the one hand, this overlapping has negligible effect on the excluded volume for the water−graphene interactions and corresponding location of the first adsorbed water layer (e.g., oxygen peak) as long as $h \geq 9$ Å. On the other hand, the effect of confinement on the behavior of the $q_T(z)$, $n_{HB}(z)$, and $n_{OO}(z)$ is rather pronounced, as illustrated in Figure 7a−c, where we should note that the strength of the tetrahedral parameter and the hydrogen bonding oscillate (in phase with each other) about the bulk value for $h \geq 15$ Å, these peaks are not in phase with the corresponding $g_O(z)$ peaks in Figure 4. For example, for $h = 15$ Å, the confined system exhibits four peaks in its $g_O(z)$, that is, two main (outermost) and two secondary adsorption layers, yet, the corresponding $q_T(z)$ and $n_{HB}(z)$ show three peaks at ~(±)2.5 Å and at the center of the slit-pore (i.e., 0.0 Å). Moreover, note that $n_{OO}(z)$ presents two peaks, with larger coordination than the corresponding bulk counterpart, at the same axial location of the secondary adsorption layers, followed by a decrease in the coordination for the adsorbed water in the main (outermost) adsorption layers. These effects are magnified by the more pronounced overlapping between the two approaching interfacial structures as the

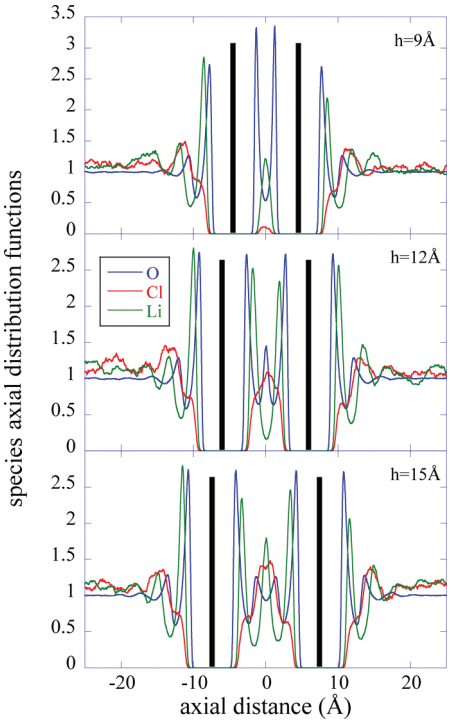

Figure 8. Axial distribution functions of species in 2*m* LiCl aqueous solutions interfacing planar graphene plates in the slit-pore configuration within the range of interplate separations $9 \leq h$ (Å) ≤ 15 at $T = 298$ K and $P = 1$ atm.

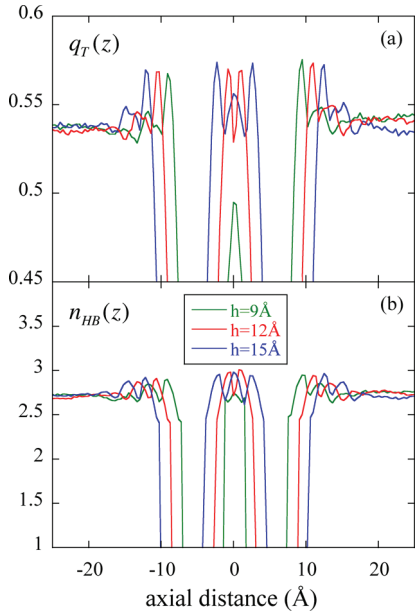

Figure 9. Axial profiles of (a) $q_T(z)$, (b) $n_{HB}(z)$ for 2*m* LiCl aqueous solutions interfacing planar graphene plates in the slit-pore configuration within the range of interplate separations $9 \leq h$ (Å) ≤ 15 at $T = 298$ K and $P = 1$ atm.

interplate separation decreases below $h = 15$ Å. In fact, for $h = 12$ Å the confined water exhibits only one peak for $n_{OO}(z)$ at the center of the slit, that is, an indication of a stronger water-coordination (∼0.3 additional molecules) than that for the corresponding bulk counterpart. However, the severe overlapping at $h = 9$ Å, that allows the accommodation of just one water layer per surface (Figure 4), becomes the onset of pronounced changes in the water microstructure, as illustrated by the significant reduction of the strength of the structural descriptors in Figure 7a−c.

The observed effect of the overlapping on the corresponding water-hydrogen peaks (i.e., in Figure 4) suggest that for $h = 15$ Å the water hydrogens in the two emerging layers are slightly off the parallel plane and point toward the center of the confined region; for $h = 12$ Å, the water hydrogens sit on the molecular plane parallel to the plates; and for $h = 9$ Å, the two water layers have one hydrogen lying on the plane containing the water−oxygen and laying parallel to the graphene plate, while the other hydrogen is pointing away from the plate, that is, resulting in a small double peak.

3.2. External versus Internal Graphene−Aqueous Electrolyte Interfacial Regions. In Figure 8 we compare the resulting axial profiles of all species distributions functions for the 2*m* solutions of LiCl within the interplate separation $9 \leq h$ (Å) ≤ 15. An outstanding feature from this comparison is that the presence of 2*m* mono- and divalent metal chloride solutions has a rather negligible effect on the "internal" (confined) axial water density distributions (Figures SI-3a-b and SI-4a-b in the Supporting Information). From a solvation viewpoint, the "internal" and "external" ion density profiles behave dramatically different as a result of the balance between confinement and ion hydration (i.e., ion−water coordination n_{OI}). In particular, note that the ions are adsorbed into the "internal" and "external" surfaces as hydrated species, that is, there is always a water layer between the ions and the graphene surface. However, as clearly illustrated in Figure 8, there is a noticeable differential behavior between the anion and the cation hydration that translates into significantly different ion−surface interaction strength with contrasting "internal" and "external" interfacial structures.

Because its small water coordination (see Figure 10c, below), the first Li^+ layers for $h > 9$ Å, are adsorbed through water-mediated interactions with both internal and external surfaces, that is, at axial positions of ∼±4 Å from the graphene surfaces (see Figure 8), while the second Li^+ layers in the "external" interfaces appear at ∼±7.4 Å from the corresponding graphene surfaces, regardless of the interplate separation. Obviously, the "internal" axial distribution of Li^+ exhibits a second layer (bottom part of Figure 8) only for $h = 15$ Å, which results from the overlapping of the interfacial structures of the left and right graphene plates, and located precisely at the center of the slit pore, that is, $0.5h = 7.5$ Å. This behavior is in contrast to that for Ba^{2+} and Y^{3+} whose larger water coordination prevents their strong adsorption at the first layer as illustrated and discussed in the Supporting Information document (i.e., Figures SI-1 and SI-2).

Finally, note that, for $h = 9$ Å, and due to obvious confinement constraints, the slit-pore can barely accommodate the hydrated ions as clearly illustrated by the profiles at the top of Figures 8−10, and consequently, the ions are expulsed from the slit-pore according to the size of their water coordination (see Discussion and corresponding figures below).

In contrast to the cations, the chloride anions barely approach the water-mediated surface, hindered by their larger solvation shell (Figure 10b and Figures SI-8b and SI-10b in the Supporting Information) and through their interaction with the surrounding cations, by settling around the second water layer where they are usually sandwiched between two layers of cations. Note, however, that for YCl_3 solutions the anion exhibits a stronger interaction

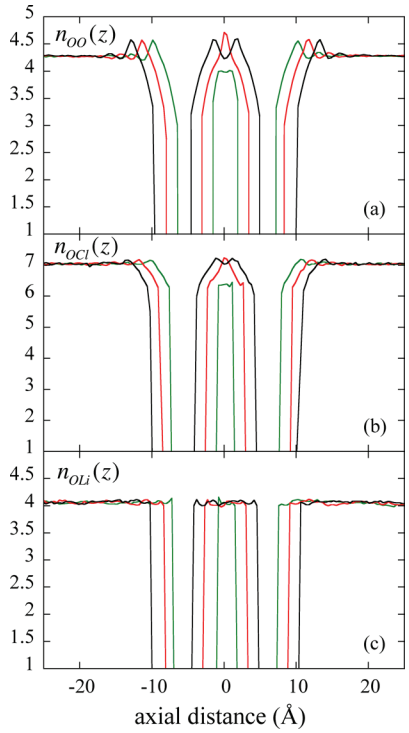

Figure 10. Axial profiles of (a) $n_{OO}(z)$, (b) $n_{OCl}(z)$, and (c) $n_{OLi}(z)$ for 2*m* LiCl aqueous solutions interfacing planar graphene plates in the slit-pore configuration within the range of interplate separations $9 \leq h$ (Å) ≤ 15 at $T = 298$ K and $P = 1$ atm.

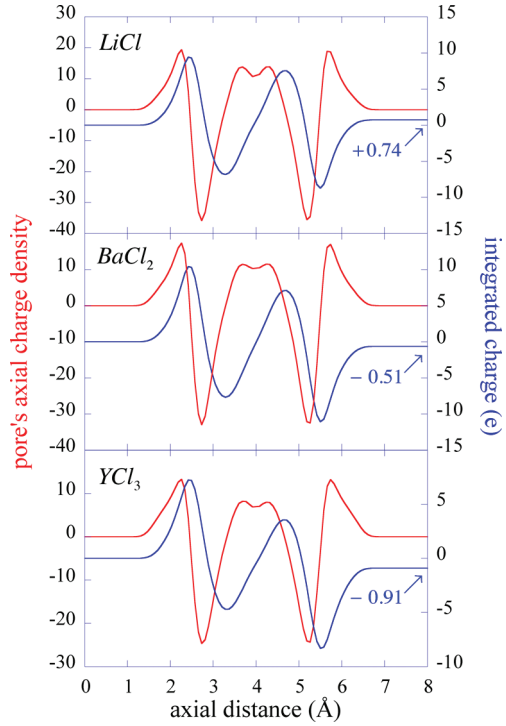

Figure 11. Axial profiles for the local charge density and its volume integrated counterpart for the aqueous solutions within the graphene slit-pore with $h = 9$ Å at $T = 298$ K and $P = 1$ atm.

with the graphene surface, that is, two small peaks between water layers and the already mentioned alternating anion−cation layering (Figure SI-2 in the Supporting Information).

As expected, the isobaric−isothermal hydration of the ionic species induces an additional structural perturbation to the interfacial water whose evidence is illustrated in Figures 9 and 10, where we plot the corresponding axial profiles for the water tetrahedral order parameter $q_T(z)$, number of hydrogen bonds $n_{HB}(z)$, and species coordination numbers $n_{O_i}(z,r_c^i)$. These figures provide clear evidence on the detrimental effects of ionic species on the tetrahedral water structure and its hydrogen-bonding network, where ionic size and charge are the major players in this phenomenon. According to these figures (see also Figure 6), 2*m* LiCl induces a clear change for the bulk water structure characterized by Δq_T(bulk), $\simeq -0.1$; Δn_{HB}(bulk), $\simeq -0.5$; and n_{OO}(bulk), $\simeq -0.25$, with n_{OLi}(bulk), $\simeq 4.0$; and n_{OCl}(bulk), $\simeq 7.0$, where these bulk values appear independent of the interplate distance *h*. The behavior of the confined water is similar to the pure water counterpart, if we shifted the corresponding properties by the changes indicate above. Note that the ionic differential hydration behavior, that is, n_{OLi}(bulk) $\simeq 4.0$ versus n_{OCl}(bulk) $\simeq 7.0$, translates into a dehydration of Cl^- with increasing confinement (see Figure 10b), followed by the gradual expulsion of the anion from the confined space (issue d of the Introduction). In contrast, Li^+ keeps its four-water coordination. The corresponding profiles for Ba^{2+} and Y^{3+} are shown and discussed in the Supporting Information.

4. DISCUSSION AND CONCLUDING REMARKS

A great deal of experimental evidence on the increased capacitance in electrochemical double layer capacitors (EDLC), including its suggested connection with ionic size and solvation behavior of the electrolyte species, comes from nanoporous carbon electrodes characterized by their high surface area.[56−58] Unfortunately, their actual geometry cannot be realistically mapped onto either cylindrical or planar interfacial representations due to unavoidable fluid−fluid and fluid−solid correlation across the system.[59] Consequently, it is highly desirable to analyze the above-suggested link starting with simpler and precisely defined interfacial systems (and their confined counterparts) to test unambiguously the validity of any conjectured effect and its underlying microscopic mechanism.

In the present study, we have chosen a simple configuration comprising an immersed finite-size plate surface that breaks the homogeneous nature of an otherwise isotropic aqueous solution through the formation of a pair of interfacial regions on each side of the plate surface, and the emerging of confinement resulting from the approach of two interfacial regions. This configuration allows the simultaneous analysis of interfacial and confinement behavior of fluids in equilibrium with their own bulk counterpart at the same global state conditions and composition. In contrast, most simulation effort on the study of interfacial and confined water and aqueous electrolyte solutions available in the literature has involved effectively closed systems, that is, where the fluid in contact with the solid surface is characterized by a fixed total density or total number of particles.[33,60−67] This choice of (closed) simulation ensembles might have unintended consequences such as the artificial enforcement of local electroneutrality within the confined fluid through ion pairing (because the system would not be able to exchange species to thermodynamically equilibrate with the corresponding bulk counterpart at the prevailing global state conditions and composition) and, thus, preclude the observation of other relevant phenomena,

including the expulsion of species and the onset of oscillation between wet and dry states.

For example, as the interplate distance becomes similar to the size of hydrated ionic species, the differential hydration behavior of these species (i.e., significant differences of hydration numbers) would prevent local electroneutrality in these open systems through the selective expulsion of ions bearing larger hydration shells from the confined spaces. In fact, according to Figure 11 where we plot the axial profiles for the charge density and the corresponding volume-integrated charge, for $h = 9$ Å the slit-pore does not become electroneutral, that is, it stays positively charged ($\sim+0.74e$) for the Li^+ solution, while negatively charged for the Ba^{2+} ($\sim-0.51e$) and Y^{3+} ($\sim-0.91e$) aqueous chloride solutions, respectively. For the area size of the graphene plates used in this work, these charges would correspond to a surface charge density in each plate of the order of $\sim+0.022C/m^2$, $\sim-0.015C/m^2$, and $\sim-0.027C/m^2$, respectively, that is, of similar magnitude as those experimentally observed.[57] The observed trend for the pore charging can be rationalized by recalling the differential hydration behavior of these cations relative to that of the anion (e.g., Figure 10b,c and Figures SI-8b-c and SI-10b-c in the Supporting Information). In fact, as illustrated in Figure SI-11 of the Supporting Information, the extent of these pore charging follows the trend of the cation's coordination number when Cl^- is the common counterion.

As the interplate spacing goes below 9 Å, and as a result of the pronounced reduction of the hydrogen bonding strength (e.g., Figures 6b and 7b), water becomes unstable and it is gradually expelled from the confined space following a dewetting process typically expected for this type of hydrophobic plates.[28,68] This instability is most clearly manifested for $h \simeq 6.25$ Å as an oscillation of the number of water molecules in the interplate region (Figure 12a) whose pore-density counterparts would represent an oscillatory transition between a vapor and a liquid phase in contact with the graphene plates. Moreover, in Figure 12b, we plot the average number of confined water molecules as a function of the geometrical confining volume, where the corresponding slope represents the average water density ρ_{pore} inside the slit pore. An outstanding feature of this representation is the lack of dependency of ρ_{pore} on the interplate separation for a wide range of confinement, that is, $9 \leq h$ (Å) ≤ 30, with $\rho_{pore} \approx \rho_{bulk}$. Moreover, note that (a) ρ_{pore} increases slightly for $h < 9$ Å before decreasing to a negligible value ($\sim V_{pore}{}^{-1}(h)$), and (b) the onset of dewetting, $h < 9$ Å, the slight increase in ρ_{pore} is clearly manifested by the strengthening of the oxygen peaks (by one unit) in the confined water depicted in Figure 4 (i.e., for $h = 9$ Å), as well as by the corresponding slope in Figure 12b.

This behavior can be rationalized by invoking Widom's potential distribution theorem for inhomogeneous fluids,[69] and the idea introduced by Heinbuch and Fischer[70] on the sampling averaging over a probe volume. In fact, because the configurational chemical potential of water (or any species for that matter) $\mu^c_{water} \equiv (\mu_{water} - \mu^{IG}_{water})_{TV}$ is uniform across the inhomogeneous system, that is, $\mu^c_{water} = kT \ln(\rho(z)/\langle\exp(-\psi/kT)\rangle_z)$ is independent of the (axial) position, then, we can formally evaluate it as if the confined fluid were a homogeneous phase characterized by the pore-averaged properties. In other words, $\mu^c_{bulk\ water} = \mu^c_{pore\ water} = kT \ln(\rho_{pore}/\overline{\langle\exp(-\psi/kT)\rangle}_{pore})$, where the pore-averaged properties are given by $\rho_{pore} \equiv h^{-1}\int_{-0.5h}^{+0.5h}\rho(z)dz$ and $\overline{\langle\exp(-\psi/kT)\rangle}_{pore} \equiv h^{-1}\int_{-0.5h}^{+0.5h}\langle\exp(-\psi/kT)\rangle_z dz$, and ψ is the so-called test particle configurational potential. Consequently, the average density ρ_{pore} and the Boltzmann factor $\overline{\langle\exp(-\psi/kT)\rangle}_{pore}$ must change "in registry", that is, an increase in ρ_{pore} would also mean a more energetically favorable test particle potential ψ. The fact that $\rho_{pore} \approx \rho_{bulk}$ for $9 \leq h$ (Å) ≤ 30 (Figure 12b) suggests that, despite the SFI overlapping, water behaves "in average" as its bulk counterpart.

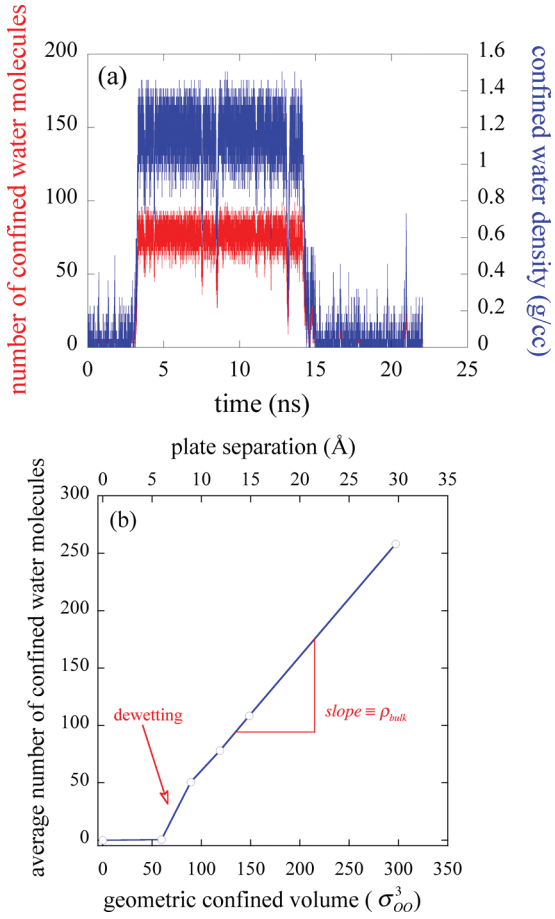

Figure 12. (a) Instantaneous number of confined water molecules for $h = 6.25$ Å, (b) average number of confined water molecules as a function of both the interplate separation and corresponding geometrical confined volume at $T = 298$ K and $P = 1$ atm.

In summary, in this work, we have addressed four fundamental issues regarding SFI behavior involving uncharged graphene plates immersed in isobaric−isothermal environments composed of either water or simple metal chlorides aqueous solutions. Our findings indicate that for pure water at ambient conditions (a) the structure of the "external" SFIs is independent of the interplate distance h in the range $0 \leq h$ (Å) ≤ 30, in striking contrast to the corresponding "internal" (confined) counterparts, consequently, (b) we find no evidence of wall-mediated correlation effect between "external" and "internal" SFIs, (c) the slit-pore dewets as the interplate separation is reduced below $h \sim 9$ Å, while for aqueous solutions (d) the differential hydration between anions and cations induces the selective expulsion of ions, which results in the charging of the slit-pore.

■ ASSOCIATED CONTENT

Ⓢ Supporting Information. Additional discussion and illustrations on the axial profiles of species densities, charge

density, relative water orientation, species coordination, hydrogen bonding strength, and tetrahedral for the barium and yttrium chloride aqueous solutions. This material is available free of charge via the Internet at http://pubs.acs.org.

AUTHOR INFORMATION

Corresponding Author
*E-mail: chialvoaa@ornl.gov. Fax: 865-574-4961.

ACKNOWLEDGMENT

This material is based upon work supported as part of the Fluid Interface Reactions, Structures and Transport (FIRST) Center, an Energy Frontier Research Center funded by the U.S. Department of Energy, Office of Science, Office of Basic Energy Sciences, under Award Number ERKCC61.

REFERENCES

(1) Stillinger, F. H. *J. Solution Chem.* **1973**, *2*, 141.
(2) Lum, K.; Chandler, D.; Weeks, J. D. *J. Phys. Chem. B* **1999**, *103*, 4570.
(3) Maibaum, L.; Chandler, D. *J. Phys. Chem. B* **2003**, *107*, 1189.
(4) Hummer, G.; Rasaiah, J. C.; Noworyta, J. P. *Nature* **2001**, *414*, 188.
(5) Werder, T.; Walther, J. H.; Jaffe, R. L.; Halicioglu, T.; Koumoutsakos, P. *J. Phys. Chem. B* **2003**, *107*, 1345.
(6) Zangi, R.; Mark, A. E. *J. Chem. Phys.* **2004**, *120*, 7123.
(7) Pertsin, A.; Grunze, M. *J. Phys. Chem. B* **2004**, *108*, 1357.
(8) Yang, X. N.; Yue, X. P. *Colloids Surf., A* **2007**, *301*, 166.
(9) Cicero, G.; Grossman, J. C.; Schwegler, E.; Gygi, F.; Galli, G. *J. Am. Chem. Soc.* **2008**, *130*, 1871.
(10) Giovambattista, N.; Debenedetti, P. G.; Rossky, P. J. *J. Phys. Chem. C* **2007**, *111*, 1323.
(11) Gordillo, M. C.; Marti, J. *J. Phys.: Condens. Matter* **2010**, *22*, 284111.
(12) Luna, M.; Colchero, J.; Baro, A. M. *J. Phys. Chem. B* **1999**, *103*, 9576.
(13) Bellissent-Funel, M. C. *Eur. Phys. J. E* **2003**, *12*, 83.
(14) Schwendel, D.; Hayashi, T.; Dahint, R.; Pertsin, A.; Grunze, M.; Steitz, R.; Schreiber, F. *Langmuir* **2003**, *19*, 2284.
(15) Steitz, R.; Gutberlet, T.; Hauss, T.; Klosgen, B.; Krastev, R.; Schemmel, S.; Simonsen, A. C.; Findenegg, G. H. *Langmuir* **2003**, *19*, 2409.
(16) Jensen, T. R.; Jensen, M. O.; Reitzel, N.; Balashev, K.; Peters, G. H.; Kjaer, K.; Bjornholm, T. *Phys. Rev. Lett.* **2003**, *90*, 086101.
(17) Pareek, A.; Torrelles, X.; Angermund, K.; Rius, J.; Magdans, U.; Gies, H. *Langmuir* **2008**, *24*, 2459.
(18) Ball, P. *Nature* **2003**, *423*, 25.
(19) Maccarini, M. *Biointerphases* **2007**, *2*, MR1.
(20) Nicholson, D.; Parsonage, N. G. *Computer Simulation and the Statistical Mechanics of Adsorption*; Academic Press: New York, 1982.
(21) Wallqvist, A.; Berne, B. J. *J. Phys. Chem.* **1995**, *99*, 2893.
(22) Huang, X.; Margulis, C. J.; Berne, B. J. *Proc. Natl. Acad. Sci. U.S. A.* **2003**, *100*, 11953.
(23) Hummer, G.; Garde, S. *Phys. Rev. Lett.* **1998**, *80*, 4193.
(24) Gordillo, M. C.; Marti, J. *J. Phys. Chem. B* **2010**, *114*, 4583.
(25) Malani, A.; Ayappa, K. G.; Murad, S. *J. Phys. Chem. B* **2009**, *113*, 13825.
(26) Castrillon, S. R. V.; Giovambattista, N.; Aksay, I. A.; Debenedetti, P. G. *J. Phys. Chem. B* **2009**, *113*, 1438.
(27) Giovambattista, N.; Debenedetti, P. G.; Rossky, P. J. *J. Phys. Chem. B* **2007**, *111*, 9581.
(28) Zangi, R.; Hagen, M.; Berne, B. J. *J. Am. Chem. Soc.* **2007**, *129*, 4678.
(29) Chandra, A. *Phys. Rev. Lett.* **2000**, *85*, 768.
(30) Guardia, E.; Marti, J.; Garcia-Tarres, L.; Laria, D. *J. Mol. Liq.* **2005**, *117*, 63.
(31) Nag, A.; Chakraborty, D.; Chandra, A. *J. Chem. Sci.* **2008**, *120*, 71.
(32) Ohkubo, T.; Konishi, T.; Hattori, Y.; Kanoh, H.; Fujikawa, T.; Kaneko, K. *J. Am. Chem. Soc.* **2002**, *124*, 11860.
(33) Ohba, T.; Kojima, N.; Kanoh, H.; Kaneko, K. *J. Phys. Chem. C* **2009**, *113*, 12622.
(34) Berendsen, H. J. C.; Grigera, J. R.; Straatsma, T. P. *J. Phys. Chem.* **1987**, *91*, 6269.
(35) Dang, L. X. *J. Chem. Phys.* **1992**, *96*, 6970.
(36) Smith, D. E.; Dang, L. X. *J. Chem. Phys.* **1994**, *100*, 3557.
(37) Aqvist, J. *J. Phys. Chem.* **1990**, *94*, 8021.
(38) Bowron, D. T.; Diaz-Moreno, S. *J. Phys. Chem. B* **2007**, *111*, 11393.
(39) Nose, S. *J. Phys. Soc. Jpn.* **2001**, *70*, 75.
(40) Okumura, H.; Itoh, S. G.; Okamoto, Y. *J. Chem. Phys.* **2007**, *126*, 084103.
(41) Steele, W. A. *Surf. Sci.* **1973**, *36*, 317.
(42) Striolo, A.; Gubbins, K. E.; Chialvo, A. A.; Cummings, P. T. *Mol. Phys.* **2004**, *102*, 243.
(43) Chialvo, A. A.; Simonson, J. M. *J. Phys. Chem. C* **2008**, *112*, 19521.
(44) Impey, R. W.; Madden, P. A.; McDonald, I. R. *J. Phys. Chem.* **1983**, *87*, 5071.
(45) Delhommelle, J.; Evans, D. J. *J. Chem. Phys.* **2001**, *114*, 6229.
(46) Baranyai, A. *J. Chem. Phys.* **2000**, *112*, 3964.
(47) Fincham, D. *Mol. Simul.* **1994**, *13*, 1.
(48) von Seggern, D. *Standard Curves and Surfaces*; CRC Press: Boca Raton, FL, 1993.
(49) Chau, P. L.; Hardwick, A. J. *Mol. Phys.* **1998**, *93*, 511.
(50) Errington, J. R.; Debenedetti, P. G. *Nature* **2001**, *409*, 318.
(51) Kumar, R.; Schmidt, J. R.; Skinner, J. L. *J. Chem. Phys.* **2007**, *126*, 204107.
(52) Wernet, P.; Nordlund, D.; Bergmann, U.; Cavalleri, M.; Odelius, M.; Ogasawara, H.; Naslund, L. A.; Hirsch, T. K.; Ojamae, L.; Glatzel, P.; Pettersson, L. G. M.; Nilsson, A. *Science* **2004**, *304*, 995.
(53) Olivares, W.; Degreve, L.; Villegas, J. C.; Lozada-Cassou, M. *Phys. Rev. E* **2002**, *65*, 061702.
(54) Jabes, B. S.; Agarwal, M.; Chakravarty, C. *J. Chem. Phys.* **2010**, *132*, 234507.
(55) Lee, S. H.; Rasaiah, J. C. *J. Phys. Chem.* **1996**, *100*, 1420.
(56) Simon, P.; Gogotsi, Y. *Nat. Mater.* **2008**, *7*, 845.
(57) Chmiola, J.; Largeot, C.; Taberna, P. L.; Simon, P.; Gogotsi, Y. *Angew. Chem., Int. Ed.* **2008**, *47*, 3392.
(58) Endo, M.; Maeda, T.; Takeda, T.; Kim, Y. J.; Koshiba, K.; Hara, H.; Dresselhaus, M. S. *J. Electrochem. Soc.* **2001**, *148*, A910.
(59) Lozada Cassou, M.; Olivares, W.; Sulbaran, B. *Phys. Rev. E* **1996**, *53*, 522.
(60) Zangi, R.; Engberts, J. *J. Am. Chem. Soc.* **2005**, *127*, 2272.
(61) Hirunsit, P.; Balbuena, P. B. *J. Phys. Chem. C* **2007**, *111*, 1709.
(62) Shao, Q.; Huang, L. L.; Zhou, J.; Lu, L. H.; Zhang, L. Z.; Lu, X. H.; Jiang, S. Y.; Gubbins, K. E.; Shen, W. F. *Phys. Chem. Chem. Phys.* **2008**, *10*, 1896.
(63) Vacha, R.; Zangi, R.; Engberts, J.; Jungwirth, P. *J. Phys. Chem. C* **2008**, *112*, 7689.
(64) Argyris, D.; Cole, D. R.; Striolo, A. *Langmuir* **2009**, *25*, 8025.
(65) Shao, Q.; Zhou, J.; Lu, L. H.; Lu, X. H.; Zhu, Y. D.; Jiang, S. Y. *Nano Lett.* **2009**, *9*, 989.
(66) Argyris, D.; Cole, D. R.; Striolo, A. *ACS Nano* **2010**, *4*, 2035.
(67) Malani, A.; Murad, S.; Ayappa, K. G. *Mol. Simul.* **2010**, *36*, 579.
(68) Eun, C.; Berkowitz, M. L. *J. Phys. Chem. B* **2010**, *114*, 13410.
(69) Widom, B. *J. Stat. Phys.* **1978**, *19*, 563.
(70) Heinbuch, U.; Fischer, J. *Mol. Simul.* **1987**, *1*, 109.